ACS OMEGA

http://pubs.acs.org/journal/acsodf Article

# Interface Influence on the Photoelectric Performance of Transition Metal Dichalcogenide Lateral Heterojunctions

Jingtao Li,[‖] Yang Ma,*[,‖] Yufo Li,[‖] Shao-Sian Li, Boxing An, Jingjie Li, Jiangong Cheng, Wei Gong, and Yongzhe Zhang*

Cite This: *ACS Omega* 2022, 7, 39187−39196 Read Online

ACCESS | Metrics & More | Article Recommendations | Supporting Information

**ABSTRACT:** The ultrathin feature of two-dimensional (2D) transition metal dichalcogenides (TMDs) has brought special performance in electronic and optoelectronic fields. When vertical and lateral heterojunctions are made using different TMD combinations, the original properties of premier TMDs can be optimized. Especially for lateral heterojunctions, their sharp interface signifies a narrow space charge region, leading to a strong in-plane built-in electric field, which may contribute to high separation efficiency of photogenerated carriers, good rectification behavior, self-powered photoelectric device construction, etc. However, due to the poor controllability over the synthesis process, obtaining a clean and sharp interface of the lateral heterojunction is still a challenge. Herein, we propose a simple chemical vapor deposition (CVD) method, which can effectively separate the growth process of different TMDs, thus resulting in good regulation of the composition change at the junction region. By this method, $MoS_2$−$WS_2$ lateral heterojunctions with sharp interfaces have been obtained with good rectification characteristics, ~$10^5$ on/off ratio, 1874% external quantum efficiency, and ~120 ms photoresponse speed, exhibiting a better photoelectric performance than that of the lateral ones with graded junctions.

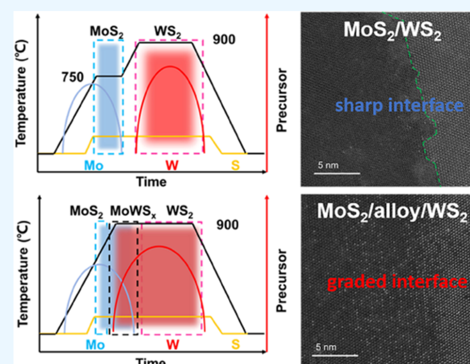


## INTRODUCTION

Two-dimensional transition metal chalcogenides (TMDs) have the characteristics of atomically thin thickness, tunable band gap, relatively high carrier mobility, etc., which can be applied in the fields of optics and electronics.[1−4] The combination of different two-dimensional (2D) TMDs can form vertical and lateral heterojunctions, tailoring the properties of primary materials and showing designable features.[5,6] For example, the built-in electric field[7,8] of the heterojunction can effectively realize the separation of photogenerated carriers[7,9] and suppress the recombination of photocarriers.[7,10−15] In addition, for these kinds of structures, characteristics including low dark current[8] and large rectification effect[16] can be usually found. However, there are interface problems to be settled for obtaining the optimal photoelectric performance of heterojunctions. As the layers are stacked by van der Waals forces in vertical heterojunctions, interlayer problems such as mismatching stacking angles,[8,12,17] contamination,[18,19] and poor coupling effects exist.[20] Compared with vertical heterojunctions, the lateral ones have more stable structures and stronger electron transport capacities due to their covalent bonds at interfaces.[21−23] These lateral heterojunctions may contribute to more complex circuit integration and serve as superlattice materials.[24,25] According to previous studies, sharp interface lateral heterojunctions are suggested, which signify a narrow space charge region and strong built-in electric field; therefore, the photoelectric properties can be expected, concluding high photogenerated carrier separation efficiency, low dark current, good rectification ratio, etc.[7,8,12,13,26] In addition to methods such as conversion,[27] phase engineering,[28,29] and doping,[30] which are applied only on preprepared TMDs for lateral heterojunction construction, chemical vapor deposition (CVD) epitaxial growth is a sequential process beginning with only reaction sources, in which large lateral sample size and mass production can be achieved, thus more suitable for sharp interface lateral heterojunction synthesis research.

Specifically, there are two different CVD epitaxial growth strategies for lateral heterojunctions: multistep CVD growth[31−33] and one-furnace CVD growth.[7,8,10,34−38] For multistep growth, when one TMD synthesis process is completed, the furnace needs to be opened and new chemical sources are supplied for subsequent growth of another TMD. This separation of growth processes allows better control over individual TMD syntheses and forbids the formation of an alloy at the interface. However, pollution and oxygen may be

Received: August 11, 2022
Accepted: September 12, 2022
Published: October 19, 2022

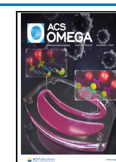

ACS Publications © 2022 The Authors. Published by American Chemical Society

introduced during the source reloading process and a large number of defects may occur, resulting in low-quality interface connection.[39−41] Therefore, the one-furnace CVD growth process is explored, in which TMD lateral heterostructures can be grown by lateral edge epitaxy without exposure to ambient conditions. As in this one-furnace CVD growth process, all sources have been put in the reaction furnace before synthesis, the source evaporation and introduction into the reaction system become crucial for the control of the composition variation at the junction region.[21,38,42−44] Hence, the controllable synthesis of lateral TMD heterojunctions with sharp interfaces and large lateral sample size remains a challenge. In this work, by analyzing the evaporation temperature of different Mo and W precursors with thermogravimetric analysis (TG), a one-furnace growth method was proposed, in which $MoO_x$/Mo foil was chosen as a molybdenum source and a $WO_3/Na_2SO_4$ mixture was used as tungsten source. According to the adjustment of the heating process, the individual $MoS_2$ and $WS_2$ growth processes can be not only separated but also overlapped effectively, resulting in monolayer $MoS_2$−$WS_2$ lateral heterojunctions with sharp and graded interfaces, for which the lateral sample size can reach 128 μm. With good rectification characteristics, ∼$10^5$ on/off ratio, 1874% external quantum efficiency, and ∼120 ms photoresponse speed of the as-prepared sharp interface $MoS_2$−$WS_2$ sample devices, it has been proved that the interface state amelioration can significantly promote the photoelectric performance of TMD lateral heterojunctions.

## METHODS

**Preparation of the Precursors.** The molybdenum metal precursor source ($MoO_x$/Mo foil) was prepared by electrochemically oxidizing a molybdenum foil (Mo, Teng shi Metal Materials, 99.99%).[45] The tungsten metal precursor source was made by mixing and grinding high-purity tungsten trioxide powder ($WO_3$, Aladdin, 99.9%) and sodium sulfate anhydrous ($Na_2SO_4$, Aladdin, 99.99%) powder in a mass ratio of 5:1, and the total powder mass was 10 mg.

**CVD Growth of Lateral Heterojunctions.** Figure 1 illustrates the growth procedure of the $MoS_2$−$WS_2$ lateral heterojunctions. The $MoO_x$/Mo precursor was placed in the center of the furnace, with the $WO_3/Na_2SO_4$ mixture powder 1 cm upstream of the $MoO_x$/Mo foil. A total of 500 mg of sulfur powder (S, Aladdin, 99.99%) was placed in the upstream position outside the furnace and heated using a heating belt, for which the temperature was set to 200 °C. The $SiO_2$/Si substrate was leaned against the side of a corundum boat over $MoO_x$/Mo and $WO_3$ precursors, with the polished side facing down. Ar was used as a carrier gas to transport precursors to the substrate; before furnace heating, it took a 500 sccm gas flow for 10 min to remove the residual air in the reaction furnace quartz tube, and then, the gas flow was turned down to 100 sccm during sample growth. To obtain sharp and graded interface heterojunctions, we set up two different heating processes. For sharp interface heterojunctions, the furnace was first heated to 750 °C and held at this temperature for 2 min and then heated to 900 °C and held at this temperature for 5 min. For graded interface ones, the furnace is heated directly to 900 °C and held at this temperature for 5 min. For both heating processes, the heating rate of the furnace was set to 30 °C per minute, and when the furnace temperature reaches 570 °C, the heating belt was turned on for the sulfur powder evaporation. After growth, the lateral heterojunction samples were collected when the furnace cooled to room temperature for further characterization.

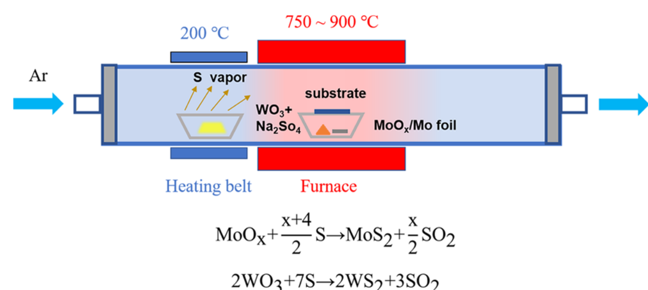


**Figure 1.** Schematic diagram of the $MoS_2$−$WS_2$ lateral heterostructure synthesized by a one-furnace CVD approach.

**Sample Characterizations.** Thermogravimetric analysis (TG) was taken with a Labsys Evo thermogravimetric analyzer. The optical images were taken with an Olympus BX 51 optical microscope. The atomic force microscopy (AFM) images were taken with a Bruker MultiMode atomic force microscope. Microstructure characterization of the samples was performed using a JEM-2100F TEM. The Raman and photoluminescence (PL) spectra were collected with a Witec Alpha 300 confocal Raman spectrometer, using a 532 laser as the excitation source.

**Device Fabrication and Measurement.** The $MoS_2$−$WS_2$ lateral heterojunction devices were fabricated by standard electron beam photolithography (SUSS MicroTec MJB4) and lift-off process. Next, 10 nm of Ti and 70 nm of Au were deposited in succession onto the substrate by e-beam evaporation (HHV FL400) followed by a lift-off process. For the specific fabrication process of $MoS_2$−$WS_2$ heterojunction devices, the details are given in Figure S3, Supporting Information. For the electrical measurement, all the devices were measured using a semiconductor analyzer (Agilent B1500A) in an atmospheric environment. For photoelectric measurements, the devices were illuminated with a supercontinuum laser (SuperK EXTREME, NKT Photonics).

## RESULTS AND DISCUSSION

Heterojunctions were grown under two different heating processes described above, and the samples were first characterized using an optical microscope, in which the inner part is $MoS_2$ and the outer part is $WS_2$. It should be noted that except the composition change of the lateral heterojunctions, the different heating processes mentioned above do not lead to obvious lateral size or distribution change for the samples; they all exhibit regular triangular shapes with uniform distribution (Figure 2a), and the lateral size of the heterostructures can reach 128 μm, as shown in Figure 2b. To analyze the photoelectric property of the lateral heterojunction, we also grew $MoS_2$ and $WS_2$ for following device characterization and comparison (shown in Figure S1, Supporting Information). For Figure 2b, the lateral interface between $MoS_2$ and $WS_2$ can be easily distinguished due to the optical contrast difference between them.[21,35] To determine whether the heterojunction is a monolayer and analyze the interface conditions, AFM characterization was performed. A typical AFM image of the lateral heterostructure is shown in Figure 2c, while the corresponding height profile along the direction of the blue arrow is shown in Figure 2d. It can be found that an estimated height of 1.1 nm with 0.1 nm fluctuations is confirmed even


https://doi.org/10.1021/acsomega.2c05151
ACS Omega 2022, 7, 39187−39196

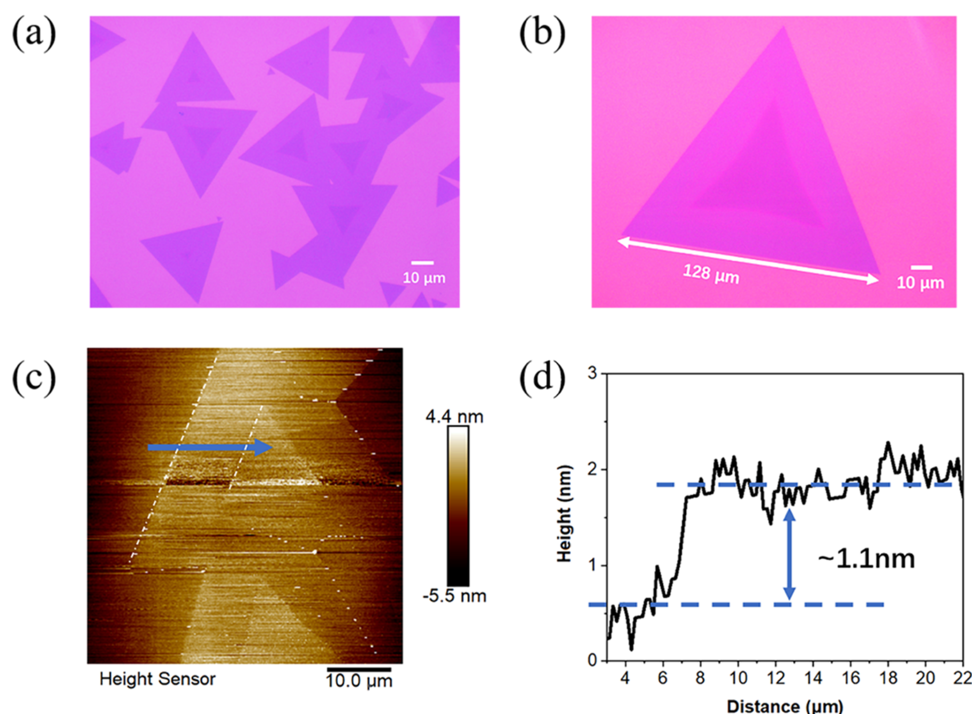


**Figure 2.** (a, b) Optical microscopy images of $MoS_2$–$WS_2$ lateral heterojunctions; (c) atomic force microscopy scanning pattern of the $MoS_2$–$WS_2$ lateral heterojunction; (d) and height curve of the blue arrow in (c).

across the interface, demonstrating that the outer $WS_2$ part of the heterojunctions has a lateral epitaxy growth at the edge of the inner $MoS_2$ nanosheet, and these two parts are both monolayers. What is more is that the surface of the heterojunction sample is very clean and smooth without any obvious deposits at the interface.

To analyze the composition variation for both sharp and graded interface lateral heterojunctions, Raman spectroscopy and PL spectroscopy characterizations have been carried out. The samples for which the heating process rested at 750 °C for 2 min before reaching 900 °C were first characterized. Figure 3a shows the optical microscopy sample image of these lateral heterojunctions; there is a clear dividing line between $MoS_2$ and $WS_2$, suggesting that they may have sharp interfaces. Figure 3c,d shows the Raman and PL spectra at five different locations (points A–E) marked in Figure 3b, respectively. The Raman spectra of points A and B show two characteristic peaks at 385 $cm^{-1}$ ($E^1_{2g}$) and 403 $cm^{-1}$ ($A_{1g}$), which are consistent with the characteristic peaks of monolayer $MoS_2$.[46] Meanwhile, the Raman spectra of two points D and E at the edge region of the lateral heterojunction show two characteristic peaks of monolayer $WS_2$ at 351 $cm^{-1}$ (${E^1}_{2g}{}^1$) and 418 $cm^{-1}$ ($A_{1g}$), respectively.[35] At the interface, the Raman spectra of point C shows the characteristic peaks of $WS_2$ and $MoS_2$ at the same time, indicating the coexistence of the two materials. Additionally, the PL spectra acquired from the mentioned five different locations show similar composition variation (Figure 3d). As 688 nm (1.8 eV) and 631 nm (2 eV) correspond to the direct excitonic emission peaks of monolayer $MoS_2$ and $WS_2$, respectively, the PL spectrum shows two peaks at the same time for the interface region (points B and C), which signifies that both $MoS_2$ and $WS_2$ exist at the two sides of the interface. It should be noticed that for point B, the 631 nm peak has begun to appear already, which is mainly due to the fact that the diameter of the laser spot is ~1 $\mu$m for PL characterization, but the point-to-point distance is less than 1 $\mu$m. To exhibit the spatial distribution of $MoS_2$ and $WS_2$ domains in the lateral heterojunction, Raman intensity mapping at 351 and 403 $cm^{-1}$ (Figure 3e–g) and PL intensity mapping at 631 and 688 nm (Figure 3h–j) have been presented. There is a clear boundary between $MoS_2$ and $WS_2$ regions, indicating that the grown lateral heterojunctions have sharp interfaces.

The lateral heterojunctions grown with a direct heating process to 900 °C, which were supposed to have a graded interface, were also characterized by Raman and PL spectra. Figure 4a shows the optical microscopy image of such a lateral heterojunction sample, in which no clear boundary between the $MoS_2$ and $WS_2$ regions can be observed. In addition, Figure 4c,d exhibits the Raman and PL spectra at five different locations (points A–E) marked in Figure 4b. Similar to the $MoS_2$–$WS_2$ lateral heterojunction with a sharp interface, at the points A and E, only the characteristic peaks for individual $MoS_2$ (385 $cm^{-1}$ ($E^1_{2g}$) and 403 $cm^{-1}$ ($A_{1g}$)) or $WS_2$ (351 $cm^{-1}$ ($E^1_{2g}$) and 418 $cm^{-1}$ ($A_{1g}$)) can be observed. However, it should be noted that even at point B, which is relatively near to the sample center, the characteristic peaks of both $MoS_2$ and $WS_2$ already appear at the same time. When the testing point continually moved from B to E, say from the inner to the outer region of the sample, the characteristic peaks of $MoS_2$ gradually weaken or even disappear. What is more is that as the points A, B, and E can represent $MoS_2$, alloy, and $WS_2$, respectively, their corresponding Raman spectra in Figure 4c have been selected for further comparison (shown in Figure S4, Supporting Information), in which an intensity enhancement of the $A_{1g}$ peak of W-doped $MoS_2$ can be seen due to the resonance of B excitons at point B.[47] For PL spectra, the peak values of A and E points are 688 nm (1.8 eV) and 631 nm (2 eV), respectively, corresponding to monolayer $MoS_2$ and $WS_2$, respectively. A decrease from 688 nm (point A) to 631 nm (point E) can be

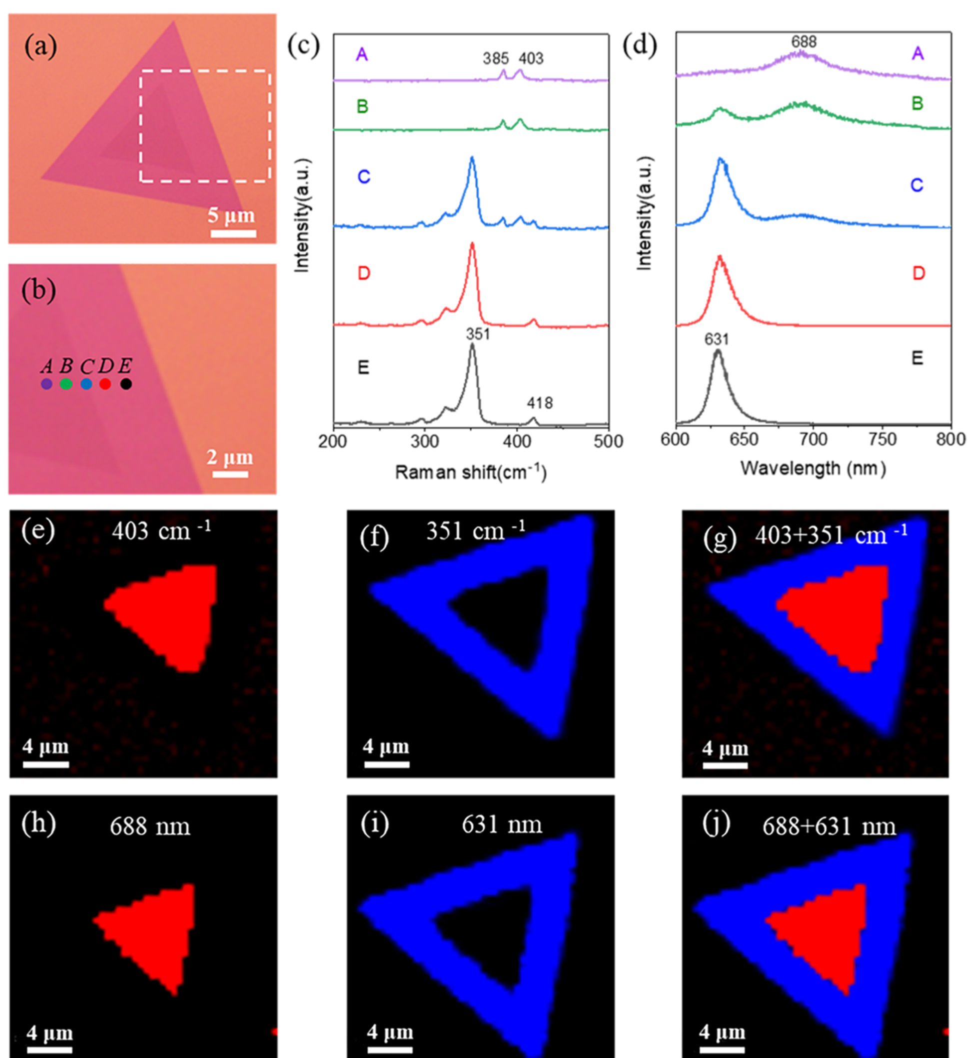


**Figure 3.** (a) Optical microscopy image of sharp interface $MoS_2$−$WS_2$ lateral heterojunctions; (b) partially enlarged image of Figure 3a; (c, d) Raman and PL spectra of five points in (b); and (e−g) Raman and (h−j) PL intensity mapping images of sharp interface $MoS_2$−$WS_2$ lateral heterojunctions.

seen, which proves that there is a Mo−W−S alloy region with lateral scale of several micrometers, in which the Mo−W composition of the alloy changes gradually with the position variation. To exhibit the junction changes of the $MoS_2$−$WS_2$ lateral graded heterojunction, Raman intensity mapping at 351 and 403 $cm^{-1}$ (Figure 4e−g) and PL intensity mapping at 631 and 688 nm (Figure 4h−j) have been presented. As mentioned above, the B exciton resonance at the alloy region leads to an intensity increase for this area in Raman mapping. Therefore, Figure 4e,f overlaps with the alloy region in Figure 4g. On the contrary, for the PL intensity mapping at 631 and 688 nm (Figure 4h−j), there is a dark interspace between the $MoS_2$ and $WS_2$ regions. This is mainly due to the fact that the difference between $MoS_2$ (688 nm) and $WS_2$ (631 nm) peaks is relatively big, and the PL peaks of their corresponding alloys vary between these two values, as shown in Figure 4d. Since the alloy area is large enough with graded composition variation, the PL mapping integrations for 688 and 631 nm have been separated effectively, and an interspace is presented, rather than an overlap, between different PL mapping regions in Figure 4j. Based on the characterization results mentioned above, it is observed that the lateral heterojunction grown with a direct heating process to 900 °C has a graded interface where the M−W−S alloy with varying compositions exists.

To further characterize the interface and the atomic structure of $MoS_2$−$WS_2$ lateral heterojunctions, high-angle annular dark-field imaging−scanning transmission election microscopy (HAADF-STEM) was performed. The high-resolution images of two different lateral heterojunctions acquired at the interface regions are shown in Figure 5a,b. Figure 5a shows a sharp interface between the monolayer $MoS_2$ and $WS_2$. Since the intensity in HAADF-STEM images is approximately proportional to the atomic number $Z^{1.7}$ and W ($Z$ = 74) atoms have higher intensity than that of Mo ($Z$ = 42) atoms due to their higher atomic number,[48] we can easily distinguish $MoS_2$ and $WS_2$ from the brightness contrast of Mo and W sites in the $Z$ contrast images, which indicates that the left part of the image is $MoS_2$ and the right part is $WS_2$. On the contrary, for the graded interface $MoS_2$−$WS_2$ lateral heterojunctions shown in Figure 5b, Mo and W atoms are mixed to form alloy regions without a clear boundary. STEM characterization results show that by selecting reaction sources and adjusting the heating process, we have successfully


https://doi.org/10.1021/acsomega.2c05151
ACS Omega 2022, 7, 39187−39196

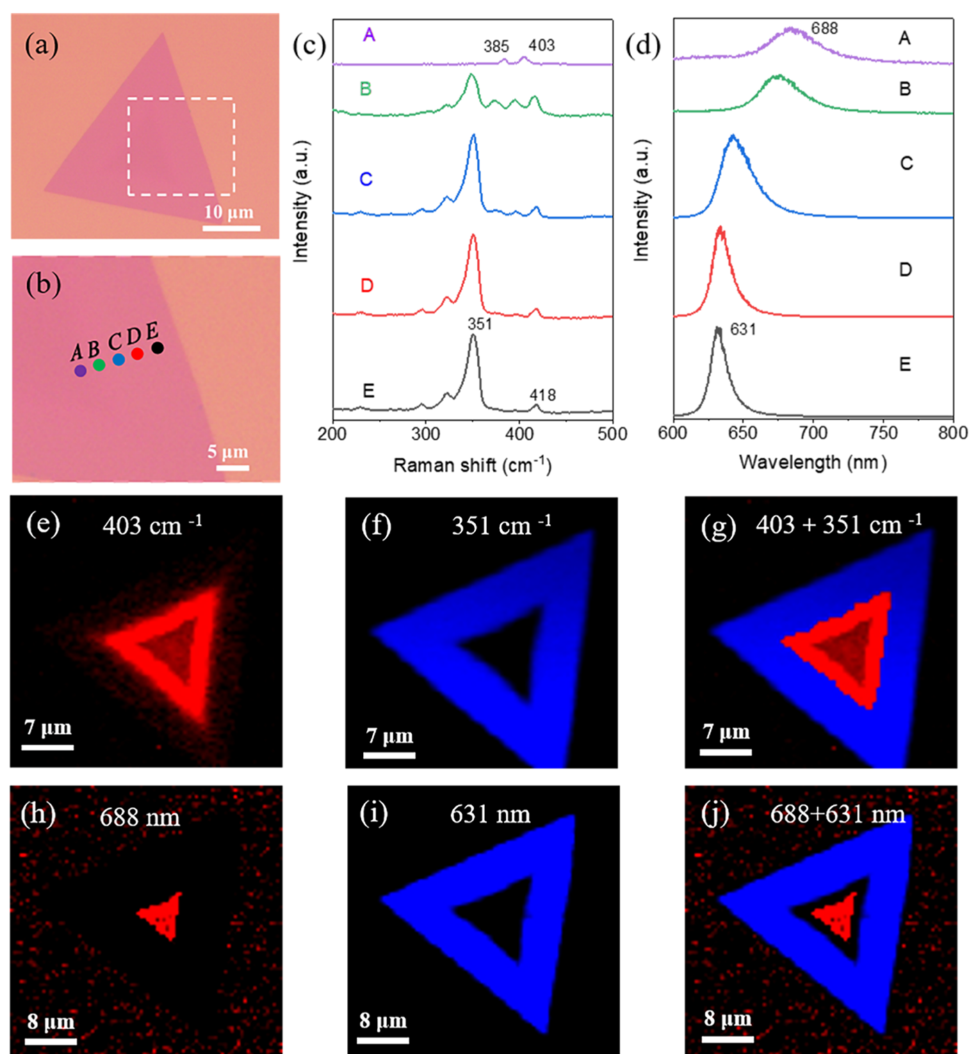


**Figure 4.** (a) Optical microscopy image of graded interface $MoS_2-WS_2$ lateral heterojunctions; (b) partially enlarged image of Figure 4a; (c, d) Raman and PL spectra of five points in (b); and (e−g) Raman and (h−j) PL intensity mapping images of graded interface $MoS_2-WS_2$ lateral heterojunctions.

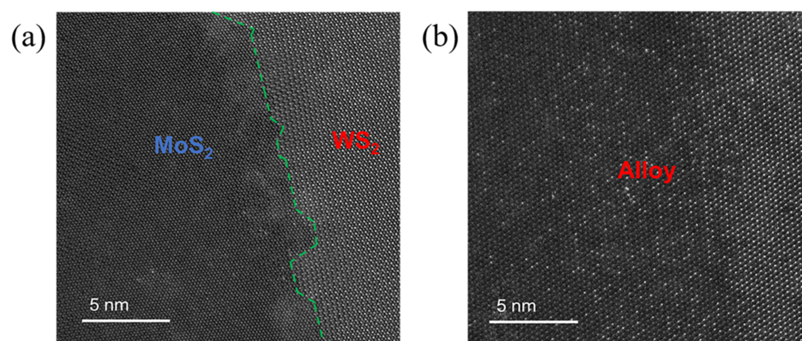


**Figure 5.** Junction structure of the $MoS_2-WS_2$ lateral heterojunction. (a) Atomic-resolution HAADF-STEM atomic structure with a sharp interface and (b) atomic-resolution HAADF-STEM atomic structure with a graded interface.

prepared both sharp and graded interface lateral $MoS_2-WS_2$ heterojunctions, respectively.

As mentioned above, the idea of source separation is key for better control of the $MoS_2-WS_2$ lateral heterojunction, resulting in not only sharp but also graded interfaces. To achieve the separated growth of $MoS_2$ and $WS_2$, the selection of the Mo source, W source, and salt is very important.[49] A thermogravimetric analysis (TG) method was used to analyze the volatilization process of different precursors, which verified $MoO_x$, $MoO_3$, the mixture of $WO_3$/NaCl, and the mixture of $WO_3/Na_2SO_4$. The TG results are shown in Figure 6a. Among the reaction sources, the $MoO_x$ foil begins to be volatilized at a low temperature (<100 °C, as shown by the red line in Figure 6a), and this source will be used up with increasing



https://doi.org/10.1021/acsomega.2c05151
ACS Omega 2022, 7, 39187−39196

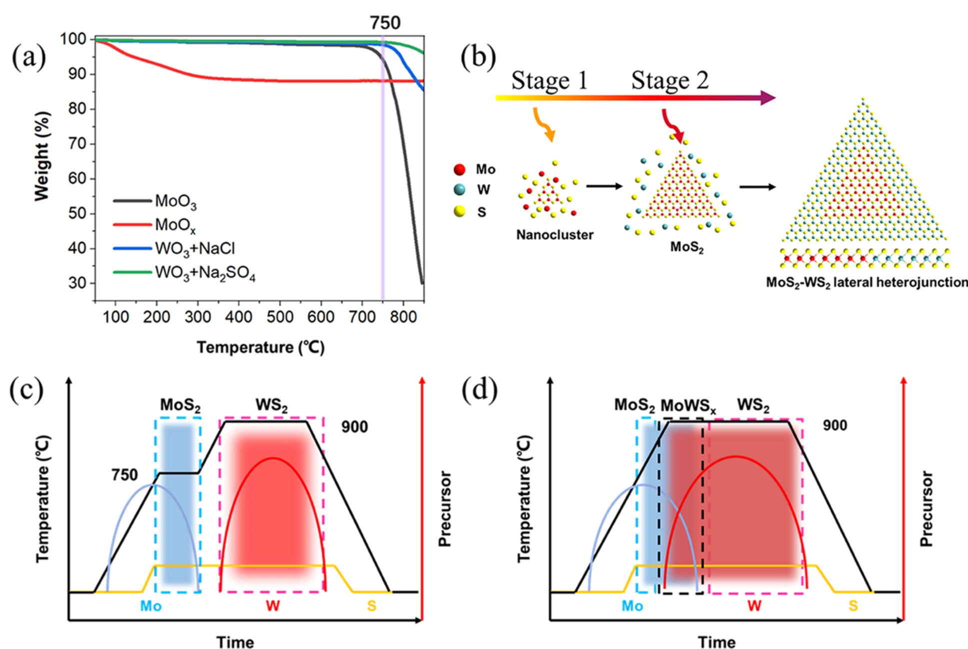


**Figure 6.** (a) Thermogravimetric analysis of different precursor sources; (b) schematic diagram of the atomic-level microgrowth process of the two-dimensional lateral heterojunction; (c) heating curve and different precursor supply of sharp interface $MoS_2$−$WS_2$ lateral heterojunctions; and (d) heating curve and supply of different precursors of graded interface $MoS_2$−$WS_2$ lateral heterojunctions. The yellow, blue, and red lines in (c) and (d) represent the heating curves of the S precursor and the amount of the Mo and W precursors evaporated onto the substrate, respectively.

temperature. However, for $MoO_3$ (black line), only when the temperature reaches 750 °C, its volatilization can be observed, and it can give a continuous supply for $MoS_2$ growth even when the W source begins to evaporate. For the W sources, their volatilization temperatures depend on the type of the added salt, in which the mixture of $WO_3$/$Na_2SO_4$ requires a highest temperature (nearly 800 °C) to be volatilized effectively. Based on this TG result, it is observed that the $MoO_x$ foil and $WO_3$/$Na_2SO_4$ mixture could be good candidates for the sharp interface lateral $MoS_2$−$WS_2$ heterojunction growth, as their corresponding volatilization temperatures differ more than 700 °C and the $MoO_x$ foil may be exhausted even before the introduction of the W source into the reaction, resulting in good separation of $MoS_2$ and $WS_2$ growth processes.

Using the $MoO_x$ foil and $WO_3$/$Na_2SO_4$ mixture as reaction sources, Figure 6b shows the growth process of the $MoS_2$−$WS_2$ lateral heterojunction. The $MoO_x$ nucleation sites were first adsorbed on the $SiO_2$/Si substrate. With the entry of the sulfur source, the $MoO_x$ nucleation sites reacted with S to form Mo−S clusters, which then grew into monolayer $MoS_2$ crystals. With a further increase of the temperature, $WO_3$ began to evaporate, and the formed W−S clusters were adsorbed on the edge of $MoS_2$, which promoted the growth of $WS_2$ and finally formed $MoS_2$−$WS_2$ lateral heterojunctions. During the process, the different heating programs determined if the junction is sharp or graded. For the heating process shown in Figure 6c, 750 °C is maintained for 2 min; during this period, $MoS_2$ starts to grow, and the $MoO_x$ foil as a Mo source will be completely consumed; thus, only pure $WS_2$ growth exists when the temperature was increased to 900 °C, resulting in the effective separation of $MoS_2$ and $WS_2$ growth, which leads to sharp interface $MoS_2$−$WS_2$ lateral heterojunctions. On the contrary, once the furnace is set to be heated directly to 900 °C and held for 5 min as shown in Figure 6d, there will not be enough time for the depletion of the Mo source, so that even when the growth of $WS_2$ begins, a certain amount of $MoO_x$ will be involved, resulting in the growth of alloyed regions. Only after the total consumption of the Mo source, can the alloyed regions change to pure $WS_2$ gradually at the edge of the $MoS_2$−$WS_2$ lateral heterojunction. The alloyed regions lead to a graded interface in this case.

It should be pointed out that this method of source separation strategy can also be applied to the growth of other TMD heterojunctions. Although there are various sources of transition metals, thanks to the molten salt growth mechanism,[49] it is suggested that with different quantities and types of salts, the evaporation temperature of transition metal precursors can be effectively adjusted, and the corresponding evaporation process can be explored by TG. Hence, the separation of different transition metal precursor evaporations can be guaranteed by selecting the appropriate combinations of precursors and salts. On this basis, the composition changes at the interface region can be regulated with control of the heating process parameters (heating rate, temperature plateau, heat preservation duration).

To assess the electrical and photoelectrical performances of the $MoS_2$−$WS_2$ lateral heterojunctions with sharp and graded interfaces, their devices have been fabricated. Such lateral structures correspond to type-II band alignment, which can be seen as p−n junctions (shown in Figure 7a,b). The current−voltage ($I$−$V$) characteristics of the two corresponding devices are shown in Figure 7c,d, with the bias ranging from −5 to 5 V. The rectification ratios of sharp and graded lateral hetero-junctions can be calculated as 378 and 151 under ± 5 V bias without gate control, for which the former value is higher than that of the previous reports.[39,50,51] The fact that the sharp junction has a better rectification behavior than that of the graded junction is mainly because the built-in electric field of the sharp junction is larger than that of the graded one, thus showing a good inhibitory effect on the reverse current.[35] What is more is that as neither individual $MoS_2$ nor $WS_2$ exhibited


https://doi.org/10.1021/acsomega.2c05151
ACS Omega 2022, 7, 39187−39196

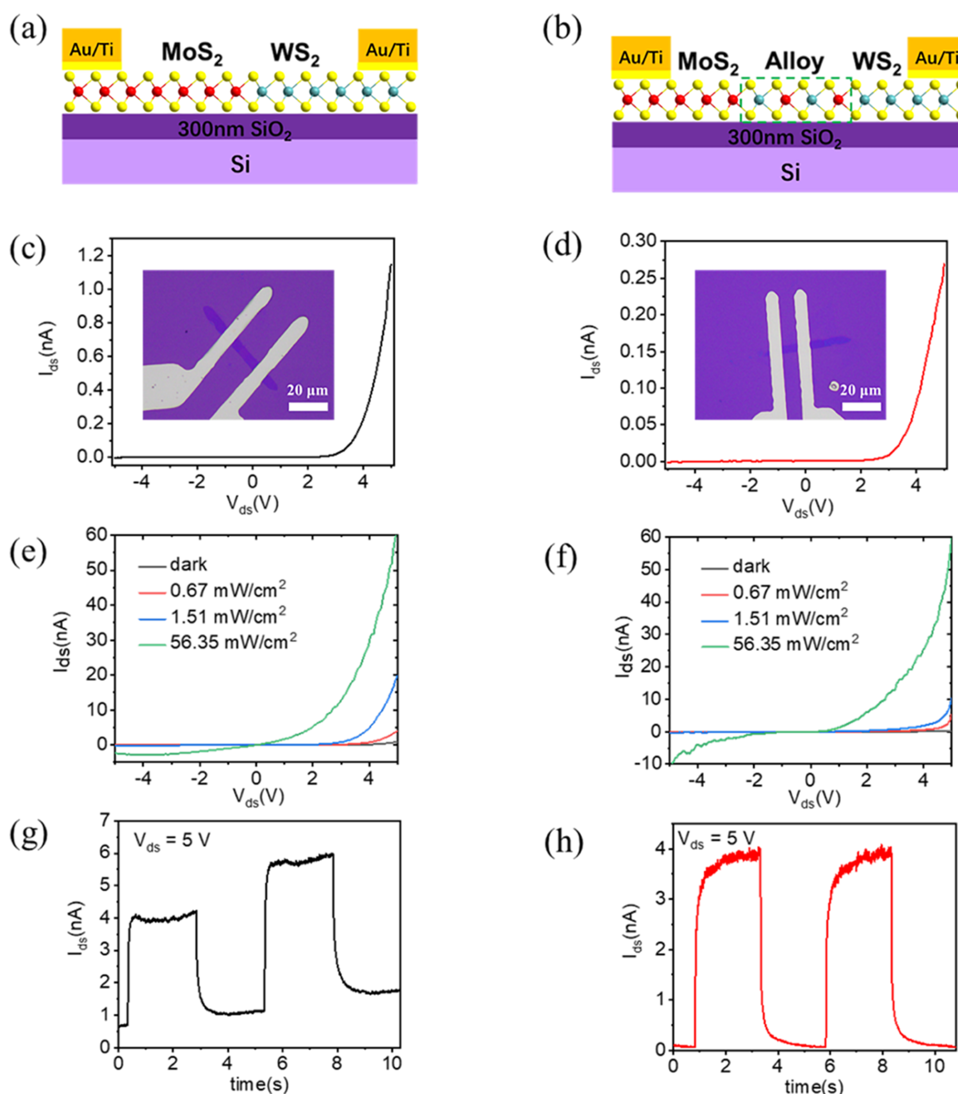


**Figure 7.** Electric and photoelectric characterization of the sharp and graded interface $MoS_2$−$WS_2$ lateral heterojunction devices. (a, b) Scheme of the sharp and graded heterostructure devices, (c, d) *I*−*V* curve of sharp and graded $MoS_2$−$WS_2$ lateral heterostructure devices. The inset shows an OM image of the device. (e, f) *I*−*V* characteristics of the p−n junction device in the dark and under illumination ($\lambda$ = 520 nm) with varying laser intensities. (g, h) Devices show photocurrent response to the light with applying a source−drain bias of 5 V. (a), (c), (e), and (g) represent sharp $MoS_2$−$WS_2$ lateral heterojunctions, (b), (d), (f), and (h) represent graded $MoS_2$−$WS_2$ lateral heterojunctions.

rectifying properties (shown in Figures S5 and S6, Supporting Information), it is confirmed that the rectifying properties of both sharp and graded interface $MoS_2$−$WS_2$ lateral heterojunctions are not due to Schottky contacts but have roots in the heterogeneous interfaces.[7,8,52] Figure 7e,f shows the *I*−*V* characteristics of the two heterojunction devices under dark and illumination conditions with varying intensities of a 520 nm laser. The photocurrent of both sharp and graded interface heterojunctions gradually increased, which was due to the photogenerated carrier concentration increase with the high-power laser density. Figure 7g,h presents the time-dependent photoresponse characteristics of the lateral heterojunction samples with a 1.51 mW $cm^{-2}$ power density incident laser. As the rise/fall time is defined as the time for the photocurrent to increase/decrease from 10 to 90 and 90 to 10%, respectively,[51] the rising and decaying time values of the sharp interface lateral heterojunctions could be estimated as ∼120 and ∼290 ms, while the rising and decaying time values of the graded ones were ∼550 and ∼230 ms, respectively. This comparison is due to the interface condition difference for the lateral heterojunctions because the alloy region of the graded junction is relatively wide and has many defects; the carriers will be affected by impurity scattering during the transmission process, resulting in a decrease in the carrier mobility and a longer response time. On the contrary, the sharp interface $MoS_2$−$WS_2$ lateral heterojunction showed relatively fast response time, thanks to its sharp and clear interface, which is even faster than that of the previous reports.[51] As the response time of individual $MoS_2$ and $WS_2$ can reach few seconds (shown in Figure S7, Supporting Information), it is proved that the lateral heterojunctions, even the graded interface ones, can improve the response time behavior of the photoelectric devices. To evaluate the on/off ratio of the as-prepared lateral heterojunction samples without illumination, their transfer characteristic curves were obtained (shown in Figure S8, Supporting Information). These curves demonstrate typical n-type behavior with $10^5$ and $10^4$ on/off ratio for sharp and graded interface $WS_2$−$MoS_2$, respectively, with $V_{ds}$ = 3 V and $V_g$ =


https://doi.org/10.1021/acsomega.2c05151
ACS Omega 2022, 7, 39187−39196

±30 V. This difference is mainly due to the fact that the off-state current of the sharp junction is smaller than that of the graded junction, which is because the sharp interface leads to a strong built-in electric field. In addition, we also estimated the responsivity, external quantum efficiency (EQE), and detectability of the photodetectors made using lateral heterostructures; the definitions for these factors are shown in the Supporting Information. With $V_{ds}$ = +5 V and incident laser density = 1.51 mW $cm^{-2}$, for the sharp and graded interface lateral heterojunctions, their responsivity could reach 7.8 and 8.2 A $W^{-1}$, corresponding to 1874 and 1966% EQE (shown in Figures S9 and S10, Supporting Information), while their detectivity values were calculated as $5.5 \times 10^{11}$ and $3.6 \times 10^{11}$ Jones, respectively. It should be noted that once the illumination intensity increased from 1.51 to 56.35 mW $cm^{-2}$, the photocurrent tended to be saturated; therefore, for the sharp and graded interface lateral heterojunctions, their responsivity, EQE, and detectability would be changed, which are 0.68/1.74 A $W^{-1}$, 164/416%, and $4.8 \times 10^{10}$/$7.5 \times 10^{10}$ Jones, respectively.

## CONCLUSIONS

In summary, a simple but effective CVD method for controlling the growth process of different TMDs has been proposed in this study, by which the interface state of lateral heterojunctions is well adjusted according to the choice of precursors and the heating process. Using this method, both sharp and graded interface $MoS_2$−$WS_2$ lateral heterojunctions with high quality and large area have been synthesized. According to the characterization results of the samples, the sharp interface $MoS_2$−$WS_2$ lateral heterojunctions had a good rectification ratio (∼378), short response time (∼120 ms), and high detectivity (∼$5.5 \times 10^{11}$ Jones), showing a better photoelectric performance than that of the ones with graded interfaces. The proposed one-furnace CVD method is universal and can be applied for other lateral heterojunction designs, which favors sharp interface formation and photoelectric performance optimization.

## ASSOCIATED CONTENT

### Supporting Information

The Supporting Information is available free of charge at https://pubs.acs.org/doi/10.1021/acsomega.2c05151.

> Optical microscopy images; Raman spectra of $MoS_2$ and $WS_2$; schematic diagram for heterojunction device fabrication; Raman spectra of $MoS_2$, alloy, and $WS_2$; electrical characterization of $MoS_2$ and $WS_2$; photoresponse of $MoS_2$ and $WS_2$; transfer characteristics of heterojunctions; responsivity, EQE, and detectivity of the heterojunctions; and definition of responsivity, external quantum efficiency, and detectability (PDF)

## AUTHOR INFORMATION


### Corresponding Authors

**Yang Ma** − *Faculty of Information Technology, Key Laboratory of Opto-Electronics Technology, Ministry of Education, Beijing University of Technology, Beijing 100124, China*; Email: mayang@bjut.edu.cn

**Yongzhe Zhang** − *Faculty of Information Technology, Key Laboratory of Opto-Electronics Technology, Ministry of Education, Beijing University of Technology, Beijing 100124, China*; orcid.org/0000-0002-3471-4402; Email: yzzhang@bjut.edu.cn

### Authors

**Jingtao Li** − *Faculty of Materials and Manufacturing, Key Laboratory of Advanced Functional Materials, Ministry of Education, Beijing University of Technology, Beijing 100124, China*

**Yufo Li** − *Faculty of Materials and Manufacturing, Key Laboratory of Advanced Functional Materials, Ministry of Education, Beijing University of Technology, Beijing 100124, China*

**Shao-Sian Li** − *Institute of Materials Science and Engineering, National Taipei University of Technology, Taipei City 10608, Taiwan*

**Boxing An** − *Faculty of Materials and Manufacturing, Key Laboratory of Advanced Functional Materials, Ministry of Education, Beijing University of Technology, Beijing 100124, China*

**Jingjie Li** − *Faculty of Materials and Manufacturing, Key Laboratory of Advanced Functional Materials, Ministry of Education, Beijing University of Technology, Beijing 100124, China*

**Jiangong Cheng** − *Faculty of Materials and Manufacturing, Key Laboratory of Advanced Functional Materials, Ministry of Education, Beijing University of Technology, Beijing 100124, China*

**Wei Gong** − *Faculty of Materials and Manufacturing, Key Laboratory of Advanced Functional Materials, Ministry of Education, Beijing University of Technology, Beijing 100124, China*

Complete contact information is available at: https://pubs.acs.org/10.1021/acsomega.2c05151


### Author Contributions

‖J.L., Y.M., and Y.L. contributed equally to this work. The article was written through contributions of all authors. All authors have given approval to the final version of the article.

### Notes

The authors declare no competing financial interest.

## ACKNOWLEDGMENTS

This work was supported by the National Natural Science Foundation of China (Nos. 62005003, 61922005, and U1930105), the General Program of Science and Technology Development Project of Beijing Municipal Education Commission (No. KM202110005008), the Cooperative Research Project of BJUT-NTUT (No. NTUT-BJUT-110-06), and the Natural Science Foundation of Beijing Municipality, China (No. JQ20027).

## REFERENCES

(1) Wang, X.; Lu, Y.; Zhang, J. Y.; Zhang, S. Q.; Chen, T. Q.; Ou, Q. Q.; Huang, J. Highly Sensitive Artificial Visual Array Using Transistors Based on Porphyrins and Semiconductors. *Small* **2021**, *17*, No. 2005491.

(2) Zhou, F. C.; Zhou, Z.; Chen, J. W.; Choy, T. H.; Wang, J. L.; Zhang, N.; Lin, Z. Y.; Yu, S. M.; Kang, J. F.; Wong, H.-S. P.; Chai, Y. Optoelectronic Resistive Random Access Memory for Neuromorphic Vision Sensors. *Nat. Nanotechnol.* **2019**, *14*, 776−782.

(3) Wang, Q. H.; Kalantar-Zadeh, K.; Kis, A.; Coleman, J. N.; Strano, M. S. Electronics and Optoelectronics of Two-Dimensional

Transition Metal Dichalcogenides. *Nat. Nanotechnol.* **2012**, *7*, 699−712.
(4) Jariwala, D.; Sangwan, V. K.; Lauhon, L. J.; Marks, T. J.; Hersam, M. C. Emerging Device Applications for Semiconducting Two-Dimensional Transition Metal Dichalcogenides. *ACS Nano* **2014**, *8*, 1102−1120.
(5) Chiu, M.-H.; Li, M.-Y.; Zhang, W. J.; Hsu, W.-T.; Chang, W.-H.; Terrones, M.; Terrones, H.; Li, L.-J. Spectroscopic Signatures for Interlayer Coupling in $MoS_2$-$WSe_2$ van der Waals Stacking. *ACS Nano* **2014**, *8*, 9649−9656.
(6) Novoselov, K. S.; Mishchenko, A.; Carvalho, A.; Castro Neto, A. H. 2D Materials and van der Waals Heterostructures. *Science* **2016**, *353*, No. aac9439.
(7) Wu, W. H.; Zhang, Q.; Zhou, X.; Li, L.; Su, J. W.; Wang, F. K.; Zhai, T. Y. Self-Powered Photovoltaic Photodetector Established on Lateral Monolayer $MoS_2$−$WS_2$ Heterostructures. *Nano Energy* **2018**, *51*, 45−53.
(8) Jia, S.; Jin, Z. H.; Zhang, J.; Yuan, J. T.; Chen, W. B.; Feng, W.; Hu, P. G.; Ajayan, P. M.; Lou, J. Lateral Monolayer $MoSe_2$ -$WSe_2$ p-n Heterojunctions with Giant Built-In Potentials. *Small* **2020**, *16*, No. 2002263.
(9) Kang, J.; Tongay, S.; Zhou, J.; Li, J. B.; Wu, J. Q. Band Offsets and Heterostructures of Two-Dimensional Semiconductors. *Appl. Phys. Lett.* **2013**, *102*, No. 012111.
(10) Gong, Y. G.; Lin, J. H.; Wang, X. L.; Shi, G.; Lei, S. D.; Lin, Z.; Zou, X. L.; Ye, G. L.; Vajtai, R.; Yakobson, B. I.; Terrones, H.; Terrones, M.; Tay, B. K.; Lou, J.; Pantelides, S. T.; Liu, Z.; Zhou, W.; Ajayan, P. M. Vertical and in-Plane Heterostructures from $WS_2$/$MoS_2$ Monolayers. *Nat. Mater.* **2014**, *13*, 1135−1142.
(11) Wang, X.; Pan, L.; Yang, J.; Li, B.; Liu, Y.-Y.; Wei, Z. Direct Synthesis and Enhanced Rectification of Alloy-to-Alloy 2D Type-II $MoS_{2(1-x)}Se_{2x}$ /$SnS_{2(1-y)}Se_{2y}$ Heterostructures. *Adv. Mater.* **2021**, *33*, No. 2006908.
(12) Zhang, X.; Huangfu, L.; Gu, Z.; Xiao, S.; Zhou, J.; Nan, H.; Gu, X.; Ostrikov, K. Controllable Epitaxial Growth of Large - Area $MoS_2$/$WS_2$ Vertical Heterostructures by Confined - Space Space Chemical Vapor Deposition. *Small* **2021**, *17*, No. 2007312.
(13) Frisenda, R.; Molina-Mendoza, A. J.; Mueller, T.; Castellanos-Gomez, A.; Van Der Zant, H. S. J. Atomically Thin p-n Junctions Based on Two-Dimensional Materials. *Chem. Soc. Rev.* **2018**, *47*, 3339−3358.
(14) Hong, X. P.; Kim, J. H.; Shi, S.-F.; Zhang, Y.; Jin, C. H.; Sun, Y. H.; Tongay, S.; Wu, J. Q.; Zhang, Y. F.; Wang, F. Ultrafast Charge Transfer in Atomically Thin $MoS_2$/$WS_2$ Heterostructures. *Nat. Nanotechnol.* **2014**, *9*, 682−686.
(15) Chen, H. L.; Wen, X. W.; Zhang, J.; Wu, T. M.; Gong, Y. J.; Zhang, X.; Yuan, J. T.; Yi, C. Y.; Lou, J.; Ajayan, P. M.; Zhuang, W.; Zhang, G. Y.; Zheng, J. R. Ultrafast Formation of Interlayer Hot Excitons in Atomically Thin $MoS_2$/$WS_2$ Heterostructures. *Nat. Commun.* **2016**, *7*, No. 12512.
(16) Duan, X. D.; Wang, C.; Shaw, J. C.; Cheng, R.; Chen, Y.; Li, H. L.; Wu, X. P.; Tang, Y.; Zhang, Q. L.; Pan, A.; Jiang, J. H.; Yu, R. Q.; Huang, Y.; Duan, X. F. Lateral Epitaxial Growth of Two-Dimensional Layered Semiconductor Heterojunctions. *Nat. Nanotechnol.* **2014**, *9*, 1024−1030.
(17) Haigh, S. J.; Gholinia, A.; Jalil, R.; Romani, S.; Britnell, L.; Elias, D. C.; Novoselov, K. S.; Ponomarenko, L. A.; Geim, A. K.; Gorbachev, R. Cross-Sectional Imaging of Individual Layers and Buried Interfaces of Graphene-Based Heterostructures and Superlattices. *Nat. Mater.* **2012**, *11*, 764−767.
(18) Li, H.; Wu, J.; Huang, X.; Yin, Z. Y.; Liu, J. Q.; Zhang, H. A Universal, Rapid Method for Clean Transfer of Nanostructures onto Various Substrates. *ACS Nano* **2014**, *8*, 6563−6570.
(19) Zhu, X. Y.; Monahan, N. R.; Gong, Z. Z.; Zhu, H. M.; Williams, K. W.; Nelson, C. A. Charge Transfer Excitons at van der Waals Interfaces. *J. Am. Chem. Soc.* **2015**, *137*, 8313−8320.
(20) Luong, D. H.; Lee, H. S.; Neupane, G. P.; Roy, S.; Ghimire, G.; Lee, J. H.; Vu, Q. A.; Lee, Y. H. Tunneling Photocurrent Assisted by Interlayer Excitons in Staggered van der Waals Hetero-Bilayers. *Adv. Mater.* **2017**, *29*, No. 1701512.
(21) Lee, J.; Pak, S.; Lee, Y.-W.; Park, Y.; Jang, A.-R.; Hong, J.; Cho, Y.; Hou, B.; Lee, S.; Jeong, H. Y.; Shin, H. S.; Morris, S. M.; Cha, S.; Sohn, J. I.; Kim, J. M. Direct Epitaxial Synthesis of Selective Two-Dimensional Lateral Heterostructures. *ACS Nano* **2019**, *13*, 13047−13055.
(22) Sun, B. F.; Chen, J. J.; Zhou, X. Y.; Liu, M.; Wu, Y. P.; Xia, Y. Z.; Li, X.; Wu, Z. M.; Kang, J. Y. Facile Synthesis of Two-Dimensional $MoS_2$/$WS_2$ Lateral Heterostructures with Controllable Core/Shell Size Ratio by a One-Step Chemical Vapor Deposition Method. *Sci. China: Phys., Mech. Astron.* **2021**, *64*, No. 107311.
(23) Zhou, Z.; Zhang, Y.; Zhang, X.; Niu, X.; Wu, G.; Wang, J. Suppressing Photoexcited Electron-Hole Recombination in $MoSe_2$/$WSe_2$ Lateral Heterostructures Via Interface-Coupled States Engineering: a Time-Domain Ab Initio Study. *J. Mater. Chem. A* **2020**, *8*, 20621−20628.
(24) Chen, K.; Wan, X.; Xie, W. G.; Wen, J. X.; Kang, Z. W.; Zeng, X. L.; Chen, H. J.; Xu, J. B. Lateral Built-In Potential of Monolayer $MoS_2$−$WS_2$ In-Plane Heterostructures by a Shortcut Growth Strategy. *Adv. Mater.* **2015**, *27*, 6431−6437.
(25) Zhang, Z. W.; Chen, P.; Duan, X. D.; Zang, K.; Luo, J.; Duan, X. F. Robust Epitaxial Growth of Two-Dimensional Heterostructures, Multiheterostructures, and Superlattices. *Science* **2017**, *357*, 788−792.
(26) Seok, H.; Megra, Y. T.; Kanade, C. K.; Cho, J.; Kanade, V. K.; Kim, M.; Lee, I.; Yoo, P. J.; Kim, H.-U.; Suk, J. W.; Kim, T. Low-Temperature Synthesis of Wafer-Scale $MoS_2$−$WS_2$ Vertical Heterostructures by Single-Step Penetrative Plasma Sulfurization. *ACS Nano* **2021**, *15*, 707−718.
(27) Mahjouri-Samani, M.; Lin, M.-W.; Wang, K.; Lupini, A. R.; Lee, J.; Basile, L.; Boulesbaa, A.; Rouleau, C. M.; Puretzky, A. A.; Ivanov, I. N.; Xiao, K.; Yoon, M.; Geohegan, D. B. Patterned Arrays of Lateral Heterojunctions within Monolayer Two-Dimensional Semiconductors. *Nat. Commun.* **2015**, *6*, No. 7749.
(28) Kappera, R.; Voiry, D.; Yalcin, S. E.; Branch, B.; Gupta, G.; Mohite, A. D.; Chhowalla, M. Phase-Engineered Low-Resistance Contacts for Ultrathin $MoS_2$ Transistors. *Nat. Mater.* **2014**, *13*, 1128−1134.
(29) Cho, S.; Kim, S.; Kim, J. H.; Zhao, J.; Seok, J.; Keum, D. H.; Baik, J.; Choe, D.-H.; Chang, K. J.; Suenaga, K.; Kim, S. W.; Lee, Y. H.; Yang, H. Phase Patterning for Ohmichomojunction Contact in $MoTe_2$. *Science* **2015**, *349*, 625−628.
(30) Nipane, A.; Karmakar, D.; Kaushik, N.; Karande, S.; Lodha, S. Few-Layer $MoS_2$ p-Type Devices Enabled by Selective Doping Using Low Energy Phosphorus Implantation. *ACS Nano* **2016**, *10*, 2128−2137.
(31) Li, M.-Y.; Shi, Y.; Cheng, C.-C.; Lu, L.-S.; Lin, Y.-C.; Tang, H.-L.; Tsai, M.-L.; Chu, C.-W.; Wei, K.-H.; He, J.-H.; Chang, W.-H.; Suenaga, K.; Li, L.-J. Epitaxial Growth of a Monolayer $WSe_2$-$MoS_2$ Lateral p-n Junction with an Atomically Sharp Interface. *Science* **2015**, *349*, 524−528.
(32) Chiu, K.-C.; Huang, K.-H.; Chen, C.-A.; Lai, Y.-Y.; Zhang, X.-Q.; Lin, E.-C.; Chuang, M.-H.; Wu, J.-M.; Lee, Y.-H. Synthesis of In-Plane Artificial Lattices of Monolayer Multijunctions. *Adv. Mater.* **2018**, *30*, No. 1704796.
(33) Liu, D. Y.; Hong, J. H.; Wang, X.; Li, X. B.; Feng, Q. L.; Tan, C. W.; Zhai, T. Y.; Ding, F.; Peng, H. L.; Xu, H. Diverse Atomically Sharp Interfaces and Linear Dichroism of 1T' $ReS_2$-$ReSe_2$ Lateral p-n Heterojunctions. *Adv. Funct. Mater.* **2018**, *28*, No. 1804696.
(34) Sahoo, P. K.; Memaran, S.; Xin, Y.; Balicas, L.; Gutierrez, H. R. One-Pot Growth of Two-Dimensional Lateral Heterostructures via Sequential Edge-Epitaxy. *Nature* **2018**, *553*, 63−67.
(35) Chen, C.; Yang, Y.; Zhou, X.; Xu, W. X.; Cui, Q. N.; Lu, J. B.; Jing, H. M.; Tian, D.; Xu, C. X.; Zhai, T. Y.; Xu, H. Synthesis of Large-Area Uniform $MoS_2$−$WS_2$ Lateral Heterojunction Nanosheets for Photodetectors. *ACS Appl. Nano Mater.* **2021**, *4*, 5522−5530.
(36) Najafidehaghani, E.; Gan, Z.; George, A.; Lehnert, T.; Ngo, G. Q.; Neumann, C.; Bucher, T.; Staude, I.; Kaiser, D.; Vogl, T.; Hübner, U.; Kaiser, U.; Eilenberger, F.; Turchanin, A. 1D p−n Junction

Electronic and Optoelectronic Devices from Transition Metal Dichalcogenide Lateral Heterostructures Grown by One-Pot Chemical Vapor Deposition Synthesis. *Adv. Funct. Mater.* **2021**, *31*, No. 2101086.

(37) Liu, D.; Hong, J.; Li, X.; Zhou, X.; Jin, B.; Cui, Q.; Chen, J.; Feng, Q.; Xu, C.; Zhai, T.; Suenaga, K.; Xu, H. Synthesis of 2H-1T′ WS2 -ReS2 Heterophase Structures with Atomically Sharp Interface via Hydrogen-Triggered One-Pot Growth. *Adv. Funct. Mater.* **2020**, *30*, No. 1910169.

(38) Zhou, J.; Tang, B.; Lin, J.; Lv, D.; Shi, J.; Sun, L.; Zeng, Q.; Niu, L.; Liu, F.; Wang, X.; Liu, X.; Suenaga, K.; Jin, C.; Liu, Z. Morphology Engineering in Monolayer $MoS_2$ -$WS_2$ Lateral Heterostructures. *Adv. Funct. Mater.* **2018**, *28*, No. 1801568.

(39) Chen, K.; Wan, X.; Wen, J. X.; Xie, W. G.; Kang, Z. W.; Zeng, X. L.; Chen, H. J.; Xu, J.-B. Electronic Properties of $MoS_2$−$WS_2$ Heterostructures Synthesized with Two-Step Lateral Epitaxial Strategy. *ACS Nano* **2015**, *9*, 9868−9876.

(40) Yoo, Y. D.; Degregorio, Z. P.; Johns, J. E. Seed Crystal Homogeneity Controls Lateral and Vertical Heteroepitaxy of Monolayer $MoS_2$ and $WS_2$. *J. Am. Chem. Soc.* **2015**, *137*, 14281−14287.

(41) Heo, H.; Sung, J. H.; Jin, G.; Ahn, J.-H.; Kim, K.; Lee, M.-J.; Cha, S.; Choi, H.; Jo, M.-H. Rotation-Misfit-Free Heteroepitaxial Stacking and Stitching Growth of Hexagonal Transition-Metal Dichalcogenide Monolayers by Nucleation Kinetics Controls. *Adv. Mater.* **2015**, *27*, 3803−3810.

(42) Huang, C.; Wu, S. F.; Sanchez, A. M.; Peters, J. J. P.; Beanland, R.; Ross, J. S.; Rivera, P.; Yao, W.; Cobden, D. H.; Xu, X. D. Lateral Heterojunctions within Monolayer $MoSe_2$-$WSe_2$ Semiconductors. *Nat. Mater.* **2014**, *13*, 1096−1101.

(43) Chen, F.; Wang, L.; Ji, X. H.; Zhang, Q. Y. Temperature-Dependent Two-Dimensional Transition Metal Dichalcogenide Heterostructures Controlled Synthesis and Their Properties. *ACS Appl. Mater. Interfaces* **2017**, *9*, 30821−30831.

(44) Zhu, J. T.; Li, W.; Huang, R.; Ma, L.; Sun, H. M.; Choi, J.-H.; Zhang, L. Q.; Cui, Y.; Zou, G. F. One-Pot Selective Epitaxial Growth of Large $WS_2$/$MoS_2$ Lateral and Vertical Heterostructures. *J. Am. Chem. Soc.* **2020**, *142*, 16276−16284.

(45) Chen, Y. F.; Deng, W. J.; Chen, X. Q.; Wu, Y.; Shi, J. W.; Zheng, J. Y.; Chu, F. H.; Liu, B. Y.; An, B. X.; You, C. Y.; Jiao, L. Y.; Liu, X. F.; Zhang, Y. Z. Carrier Mobility Tuning of $MoS_2$ by Strain Engineering in CVD Growth Process. *Nano Res.* **2021**, *14*, 2314−2320.

(46) Li, T. T.; Guo, W.; Ma, L.; Li, W. S.; Yu, Z. H.; Han, Z.; Gao, S.; Liu, L.; Fan, D. X.; Wang, Z. X.; Yang, Y.; Lin, W. Y.; Luo, Z. Z.; Chen, X. Q.; Dai, N. X.; Tu, X. C.; Pan, D. F.; Yao, Y. G.; Wang, P.; Nie, Y. F.; Wang, J. L.; Shi, Y.; Wang, X. R. Epitaxial Growth of Wafer-Scale Molybdenum Disulfide Semiconductor Single Crystals on Sapphire. *Nat. Nanotechnol.* **2021**, *16*, 1201−1207.

(47) Chen, Y. F.; Xi, J. Y.; Dumcenco, D. O.; Liu, Z.; Suenaga, K.; Wang, D.; Shuai, Z. G.; Huang, Y.-S.; Xie, L. M. Tunable Band Gap Photoluminescence from Atomically Thin Transition-Metal Dichalcogenide Alloys. *ACS Nano* **2013**, *7*, 4610−4616.

(48) Zhang, L. L.; Wang, G.; Zhang, Y.; Cao, Z. P.; Wang, Y.; Cao, T. J.; Wang, C.; Cheng, B.; Zhang, W. Q.; Wan, X. G.; Lin, J. H.; Liang, S.-J.; Miao, F. Tuning Electrical Conductance in Bilayer $MoS_2$ through Defect-Mediated Interlayer Chemical Bonding. *ACS Nano* **2020**, *14*, 10265−10275.

(49) Zhou, J. D.; Lin, J. H.; Huang, X. W.; Zhou, Y.; Chen, Y.; Xia, J.; Wang, H.; Xie, Y.; Yu, H. M.; Lei, J. C.; Wu, D.; Liu, F. C.; Fu, Q. D.; Zeng, Q. S.; Hsu, C.-H.; Yang, C. L.; Lu, L.; Yu, T.; Shen, Z. X.; Lin, H.; Yakobson, B. I.; Liu, Q.; Suenaga, K.; Liu, G. T.; Liu, Z. A Library of Atomically Thin Metal Chalcogenides. *Nature* **2018**, *556*, 355−359.

(50) Xue, Y. Z.; Zhang, Y. P.; Liu, Y.; Liu, H. T.; Song, J. C.; Sophia, J.; Liu, J. Y.; Xu, Z. Q.; Xu, Q. Y.; Wang, Z. Y.; Zheng, J. L.; Liu, Y. Q.; Li, S. J.; Bao, Q. L. Scalable Production of a Few-Layer $MoS_2$/$WS_2$ Vertical Heterojunction Array and Its Application for Photodetectors. *ACS Nano* **2016**, *10*, 573−580.

(51) Li, C. H.; Zhu, J. T.; Du, W.; Huang, Y. X.; Xu, H.; Zhai, Z. G.; Zou, G. F. The Photodetectors Based on Lateral Monolayer $MoS_2$/$WS_2$ Heterojunctions. *Nanoscale Res. Lett.* **2021**, *16*, No. 123.

(52) Woods, J. M.; Jung, Y.; Xie, Y. J.; Liu, W.; Liu, Y. H.; Wang, H. L.; Cha, J. J. One-Step Synthesis of $MoS_2$/$WS_2$ Layered Heterostructures and Catalytic Activity of Defective Transition Metal Dichalcogenide Films. *ACS Nano* **2016**, *10*, 2004−2009.



https://doi.org/10.1021/acsomega.2c05151
*ACS Omega* 2022, 7, 39187−39196